nature physics

Article

https://doi.org/10.1038/s41567-025-02997-4

Strongly interacting Hofstadter states in magic-angle twisted bilayer graphene

Received: 1 August 2024

Accepted: 14 July 2025

Published online: 11 August 2025

Check for updates

Minhao He [1,2,9] ✉, Xiaoyu Wang [3,9], Jiaqi Cai [1], Jonah Herzog-Arbeitman [2], Ran Peng [3], Takashi Taniguchi [4], Kenji Watanabe [5], Ady Stern [6], B. Andrei Bernevig [2], Matthew Yankowitz [1,7] ✉, Oskar Vafek [3,8] ✉ & Xiaodong Xu [1,7] ✉

Magic-angle twisted bilayer graphene hosts a variety of strongly correlated states at partial fillings of its flat bands. In a magnetic field, these flat bands evolve into a Hofstadter spectrum renormalized by strong Coulomb interactions. Here we study the interacting Hofstadter states that spontaneously form within the topological magnetic sub-bands of an ultraclean magic-angle twisted bilayer graphene device, including symmetry-broken Chern insulator states and fractional quantum Hall states. The observed symmetry-broken Chern insulator states form a cascade, with their Chern numbers mimicking the main sequence of correlated Chern insulators. The fractional quantum Hall states form in a Jain sequence. However, they disappear at high magnetic field, in contrast to conventional fractional quantum Hall states that strengthen with increasing magnetic field. We reveal a magnetic-field-driven phase transition from composite fermion phases to a dissipative Fermi liquid. Our theoretical analysis of the magnetic sub-bands hosting the fractional quantum Hall states predicts non-uniform quantum geometric properties far from the lowest Landau level. This points towards a more natural interpretation of these states as in-field fractional Chern insulators of the magnetic sub-bands.

The Hofstadter butterfly[1] is a general term describing the recursive energy band spectrum for electrons confined to two dimensions and with a magnetic length l_B comparable to the lattice periodicity. A new class of topologically ordered states, termed in-field Chern insulators, emerges upon fully filling a set of the magnetic sub-bands within the Hofstadter butterfly[2]. Each such gapped state is characterized by an integer total Chern number t and integer moiré band filling factor s associated with its limit following the gap to zero magnetic field. Strongly correlated states, beyond those predicted within the non-interacting Hofstadter butterfly, can also emerge when Coulomb interactions become comparable to or exceed the width of the magnetic sub-bands. These interacting Hofstadter states arise upon partially filling the magnetic sub-bands and can be categorized into two distinct classes: those with fractional s and integer t and those with fractional t and non-zero s. The former generally correspond to symmetry-broken Chern insulator (SBCI) states that enlarge the unit cell by spontaneously breaking the discrete translational symmetry of the moiré lattice[3,4]. The latter states instead result from electrons fractionalized into anyons and correspond to in-field fractional Chern insulator (FCI) states of the magnetic sub-bands[4]. Interactions could also generate states that exhibit

[1]Department of Physics, University of Washington, Seattle, WA, USA. [2]Department of Physics, Princeton University, Princeton, NJ, USA. [3]National High Magnetic Field Lab, Tallahassee, FL, USA. [4]Research Center for Materials Nanoarchitectonics, National Institute for Materials Science, Tsukuba, Japan. [5]Research Center for Electronic and Optical Materials, National Institute for Materials Science, Tsukuba, Japan. [6]Department of Condensed Matter Physics, Weizmann Institute of Science, Rehovot, Israel. [7]Department of Materials Science and Engineering, University of Washington, Seattle, WA, USA. [8]Department of Physics, Florida State University, Tallahassee, FL, USA. [9]These authors contributed equally: Minhao He, Xiaoyu Wang. ✉e-mail: minhaohe@princeton.edu; myank@uw.edu; vafek@magnet.fsu.edu; xuxd@uw.edu

https://doi.org/10.1038/s41567-025-02997-4

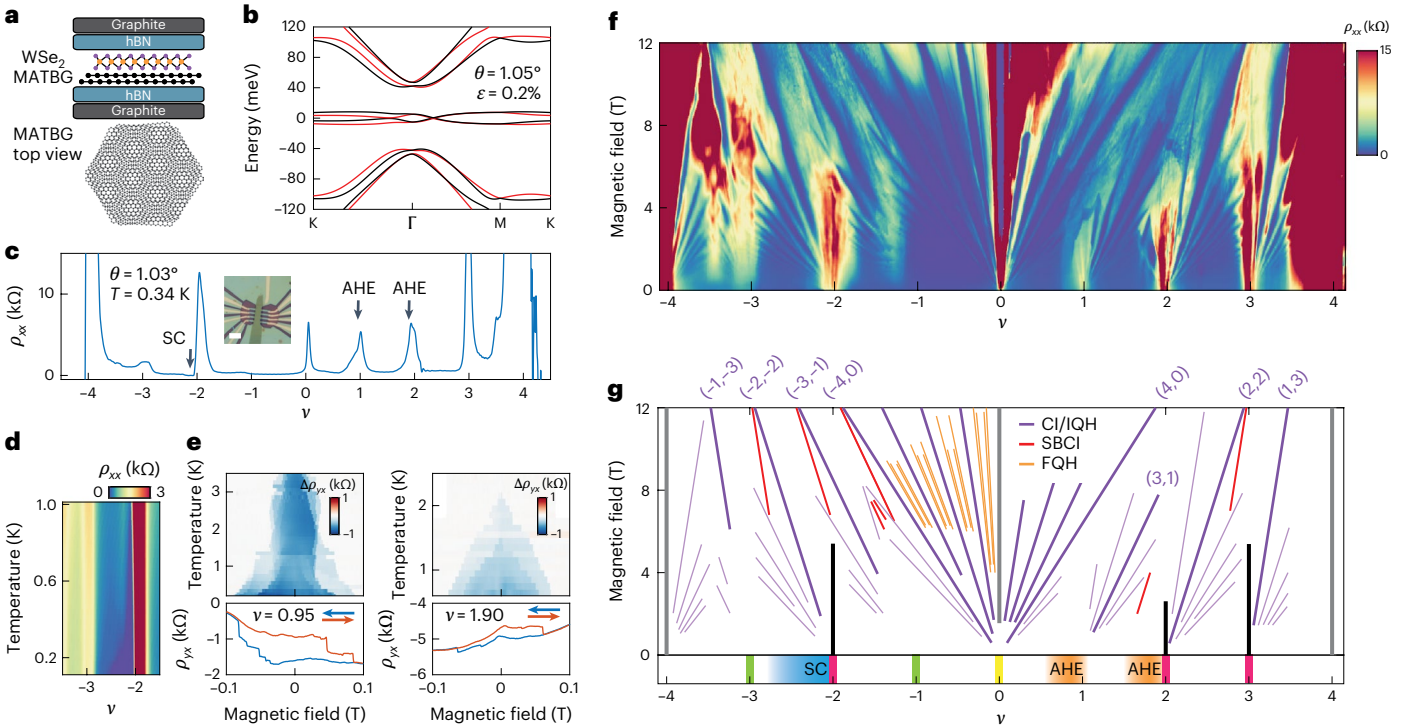

Fig. 1 | Transport characterization of a $\theta = 1.03°$ high-quality MATBG/WSe_2 sample. a, Schematic of the device structure. **b**, Flat bands of the MATBG calculated at twist angle $\theta = 1.05°$ for uniaxial heterostrain strength $\varepsilon = 0.2\%$ and orientation $\varphi = 0°$ (see Supplementary Information for details). **c**, ρ_{xx} versus ν measured at $T = 340$ mK. Regions of observed superconductivity and anomalous Hall effects are denoted by arrows. Inset: optical micrograph of the sample. **d**, Temperature dependence of ρ_{xx} in the vicinity of superconductivity. **e**, Measurements of ρ_{yx} as B is swept back and forth. Anomalous Hall effects appear near $\nu = 1$ (left panels) and $\nu = 2$ (right panels). The top panels show the amplitude of the hysteresis loop, $\Delta\rho_{yx} = \rho_{yx}^{B\downarrow} - \rho_{yx}^{B\uparrow}$, acquired as functions of temperature. The bottom panels show line traces measured at $T = 300$ mK. **f**, Landau fan diagram of ρ_{xx} measured up to 12 T at $T = 300$ mK (the corresponding ρ_{yx} is shown in Supplementary Fig. 3, along with measurements from a different contact pair). **g**, Schematic diagram indicating the different phases seen in the devices. At zero magnetic field, we denote superconductivity with the blue rectangle and regions exhibiting the anomalous Hall effect with orange. Tentative assignments of the correlated states at integer fillings are also denoted: gapped incommensurate Kekulé spiral states (magenta), gapless incommensurate Kekulé spiral states (green) and a semimetallic phase (yellow). At finite field, we denote Chern insulators and integer quantum Hall states with purple lines, SBCI states with red, FQH states with yellow and the topologically trivial insulators states with black. Scale bar, 5 μm. AHE, anomalous Hall effect; CI, Chern insulator; IQH, integer quantum Hall state; SC, superconductivity.

the coexistence of charge fractionalization and a SBCI[4], necessarily arising at both fractional s and t.

SBCI states and in-field FCI states have been seen previously in moiré superlattices of monolayer or Bernal bilayer graphene aligned with hexagonal boron nitride (hBN)[3,4]. However, these moiré lattices require extremely high magnetic fields of $B \gtrsim 20$ T, owing to their large electronic band dispersions at zero field. By contrast, the flat electronic bands of magic-angle twisted bilayer graphene (MATBG)[5–11], and other twisted graphene multilayers, greatly enhance the strength of Coulomb interactions and promote the formation of correlated states at much lower B[12–16]. In MATBG, fingerprints of strong interactions at finite magnetic field have been seen in the form of a characteristic sequence of correlated Chern insulators (CCIs)[13,17–21]. Regardless of slight differences in twist angle and microscopic strain distribution, twisted bilayer graphene devices near the magic angle always exhibit similar CCIs, having Chern numbers $|t| = 1$, 2 and 3 with moiré filling factors $|s| = 3$, 2 and 1, respectively. Theoretically reproducing this robust experimental feature has only recently been achieved in an interacting Hofstadter calculation[22] that includes uniaxial heterostrain. Experimentally, only limited experimental attention[8,12–14] has been given to gaining an understanding of the correlated Hofstadter states with fractional t or s arising within the interaction-renormalized magnetic sub-bands.

By studying an ultra-high-quality MATBG device, we report the observation of a cascade of SBCI states that forms primarily upon hole-doping its magnetic sub-bands. The sequence of Chern numbers of these states is closely connected to the parent CCI states, in that both form a cascade where the Chern number $|t|$ changes in increments of 1. These sequences are captured well by a self-consistent Hartree–Fock calculation of the interacting Bistritzer–MacDonald model in a finite magnetic field. We additionally see a sequence of fractional quantum Hall (FQH) states (fractional t and $s = 0$) that form within the magnetic sub-bands emanating from the charge neutrality point. Although these states follow the usual Jain sequence[23] and have previously been sighted in MATBG[8], their appearance in the regime where the magnetic length is comparable to the moiré periodicity marks a key distinction from FQH states seen in typical Landau levels (LLs), pointing to their unconventional nature. This is experimentally signified by the phase transitions from FQH states into a normal Fermi liquid. This behaviour is in strong contrast to the usual monotonically enhanced FQH states in crystalline graphene and most other two-dimensional electronic gases. Our Hartree–Fock band analysis shows that these fractional states arise out of strained magnetic sub-bands with finite bandwidth and non-uniform, non-ideal quantum geometric properties. Unlike in pristine LLs, this unusual quantum geometric structure points to a potential description of these states within the framework of magnetic field-induced FCIs.

High-quality MATBG/WSe_2 sample and its Landau fan diagram

We focus our attention on a MATBG device with a twist angle of $\theta = 1.03°$ (Fig. 1a,b). It has been argued that the presence of monolayer WSe_2 stabilizes the twist angle and reduces the resulting moiré disorder[24,25]. Figure 1c shows the longitudinal resistivity ρ_{xx} versus the moiré filling

https://doi.org/10.1038/s41567-025-02997-4

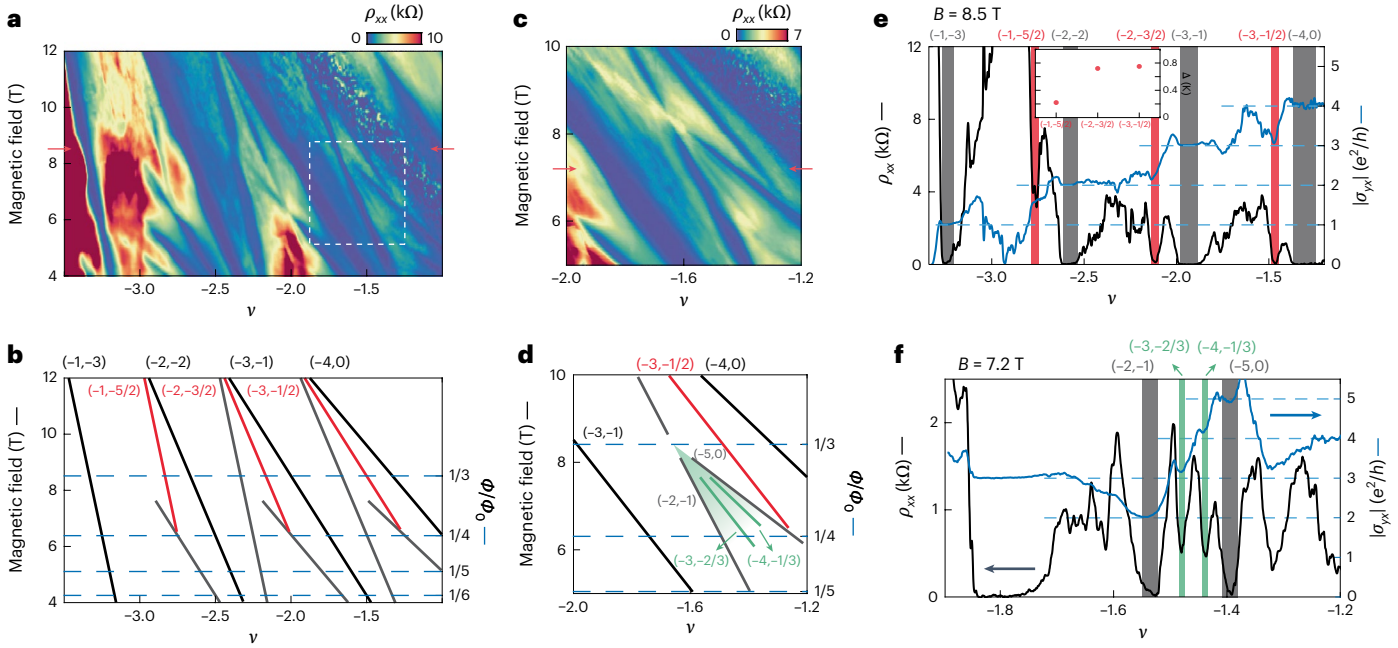

Fig. 2 | Cascades of SBCI states. a, Zoom-in measurement of the ρ_{xx} Landau fan focusing on the SBCI states on the hole-doped side. **b**, Schematic diagram of the most robust gapped states. The left *y* axis shows the corresponding magnetic flux ratio, Φ/Φ_0. **c**, Further zoom-in of the region denoted by the white dashed box in **a**. **d**, Schematic diagram of the most robust gapped states. The green shading indicates a magnetic sub-band with a total Chern number of −3. **e**, $|\sigma_{yx}|$ (right axis) and ρ_{xx} (left axis) measured at $B = 8.5$ T (red arrows in **a**). Shaded regions mark the SBCI states (red) and the main-sequence CCIs (grey). Inset: measurements of the thermal activation gap of the three SBCI states denoted in **b**. **f**, The same measurement at $B = 7.2$ T (red arrows in **c**). The green shading indicates the SBCI states seen in **d**.

factor ν measured at a temperature $T = 340$ mK (see Supplementary Fig. 1 for the temperature dependence). In addition to the correlated insulating states at $\nu = -2$, +2 and +3, we observe superconductivity at slight hole doping of $\nu = -2$ (Fig. 1d) and orbital ferromagnetism[26] associated with anomalous Hall effects near $\nu = +1$ and +2 (Fig. 1e). Both instances of the anomalous Hall effect show typical hysteresis loops in the Hall resistance ρ_{yx} with an amplitude of approximately 1 kΩ (see Supplementary Fig. 2 for the dependence on ν). Overall, our observations are consistent with previous studies of MATBG, both with[24,27,28] and without[29–31] a WSe_2 substrate.

The simultaneous observation of superconductivity and the anomalous Hall effect in a single device is rare[24,29] and partially signifies the high sample quality. The unprecedented homogeneity of our device is best reflected in the rich Landau fan diagrams of both ρ_{xx} and ρ_{yx} (Fig. 1f and Supplementary Fig. 3). A comprehensive phase diagram at both zero and finite magnetic field is shown in Fig. 1g. The Hofstadter states at finite magnetic field are identified by the simultaneous suppression of ρ_{xx} and quantization of ρ_{yx} to values of h/te^2, corresponding to their Chern number t, where h is the Planck constant. States without fully quantized ρ_{yx} are identified by the slope of their trajectories defined by the Streda formula[32], $t = (h/e)(\partial n/\partial B)$. Integer quantum Hall states and in-field Chern insulators having both integer t and s form the primary features of the Landau fan at finite magnetic field and are represented by purple lines in the schematic (see also the Landau fan at 2 K in Supplementary Fig. 4). Close inspection of the fan diagram further reveals strongly correlated states beyond the single-particle Hofstadter spectrum, including numerous SBCI states (red lines) and FQH states (yellow lines). We will elaborate on the nature of these states in the remainder of our discussion.

Cascades of SBCIs

Figure 2a,c shows high-resolution zoom-ins of two groups of SBCI states observed on the hole-doped side of the Landau fan (see ρ_{yx} in Supplementary Fig. 5), with the most robust gapped states denoted schematically in Fig. 2b,d, respectively. In addition to the conventional hierarchy of CCIs reported across many devices previously, we see an associated cascade of SBCI states indicated by the red lines in Fig. 2b. Notably, these states exhibit the same cascading sequence of Chern numbers ($t = -3$, −2 and −1) as their adjacent parent CCI but with half-integer moiré filling indices ($s = -1/2$, −3/2 or −5/2). We adopt the notation (t, s) for simplicity in referencing each of these states. Figure 2e shows line cuts of ρ_{xx} and the Hall conductivity σ_{yx} calculated from $\sigma_{yx} = \rho_{yx}/(\rho_{yx}^2 + \rho_{xx}^2)$ at $B = 8.5$ T. The (−2, −3/2) and (−3, −1/2) SBCI states are almost perfectly developed, with vanishing ρ_{xx} and nearly quantized σ_{yx}, whereas the (−1, −5/2) SBCI is clearly visible in the Landau fan but is not fully quantized. We determine the associated energy gaps Δ (Fig. 2e inset and Supplementary Fig. 6) from the thermal activation behaviour of $\rho_{xx} \propto e^{\Delta/2k_BT}$, where k_B is the Boltzmann constant. We find that the (−2, −3/2) and (−3, −1/2) states have energy gaps about three times larger than that of the (−1, −5/2) state. The results from the former two states are consistent with previous studies[13,14]. Together, these three SBCI states form a cascade with an equal interval of $\Delta t = -1$ and $\Delta s = 1$ between each state, exactly as describes the main sequence of CCIs but shifted by a fractional moiré filling factor $s_0 = 1/2$. These SBCI states can be understood as maintaining the same spin and valley polarization properties of their parent CCI[13] but further breaking the moiré lattice translational symmetry by forming a charge density wave that spontaneously doubles the unit cell area[10].

Intriguingly, we find that these three SBCI states disappear at the same lower threshold of the magnetic field, corresponding to a simple rational flux ratio $\Phi/\Phi_0 = 1/4$. A second group of SBCI states, (−3, −2/3) and (−4, −1/3), are also closely tied with a simple rational flux ratio $\Phi/\Phi_0 = 1/3$ (Fig. 2c,d,f and Supplementary Fig. 6). These two SBCI states are flanked by the (−2, −1) and (−5, 0) Chern insulators. Together, these bound a magnetic sub-band with Chern number $C = -3$ emanating from $\Phi/\Phi_0 = 1/3$ towards zero field (green-shaded region). The two SBCI states can be intuitively understood as partitioning the $C = -3$ sub-band into three parts, each with C = −1. Note that we do not

https://doi.org/10.1038/s41567-025-02997-4

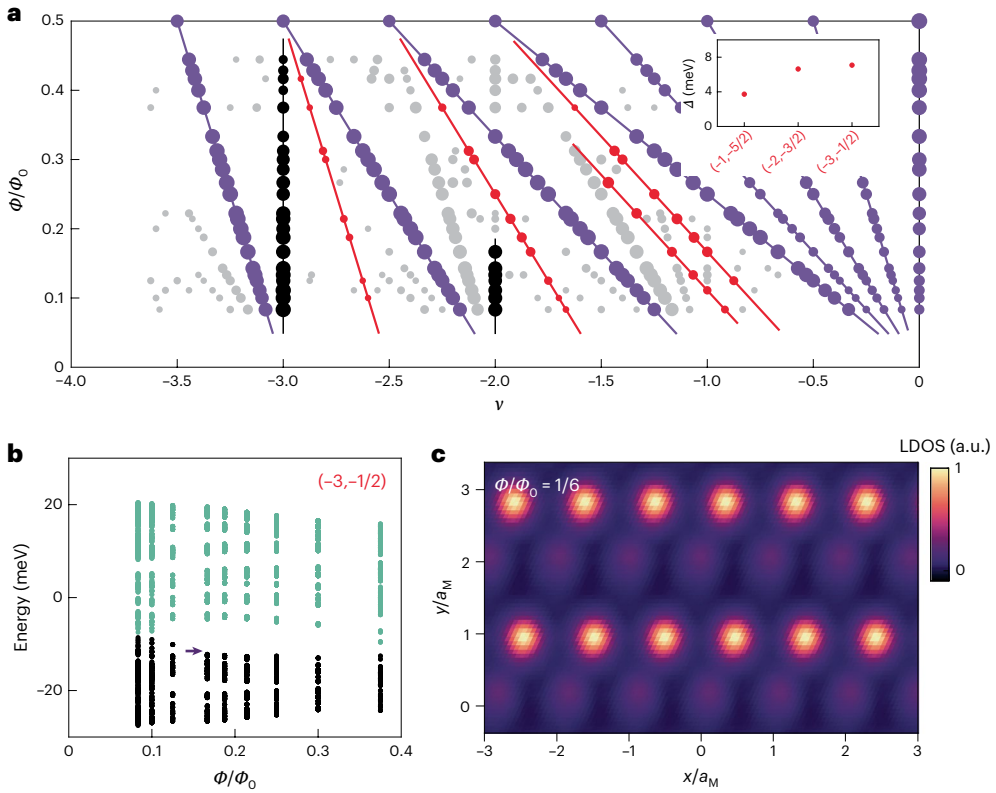

Fig. 3 | Finite-field Hartree–Fock calculation of the SBCI states. a, Calculated gapped states at finite magnetic field. The marker size is proportional to the gap size at each filling factor ν and magnetic flux ratio Φ/Φ_0. The gapped states originating from integer values of ν are denoted by purple and grey. Purple states here match the states denoted in purple in Fig. 1g. The SBCI states are denoted by red. Robust topologically trivial states are denoted by black. Inset: calculated gap size of the three SBCIs at $\Phi/\Phi_0 = 3/10$. **b**, Interacting Hofstadter spectrum when the Fermi energy is in the gap of the (−3, −1/2) state. Occupied and unoccupied states are in black and green, respectively. **c**, Local density of states calculated for the valence band edge of the (−3, −1/2) SBCI state at $\Phi/\Phi_0 = 1/6$ (purple arrow in **b**). $a_M \equiv \sqrt{|\mathbf{L}_1||\mathbf{L}_2|}$ is the effective periodicity of the strained moiré superlattice, where $|\mathbf{L}_1|$ and $|\mathbf{L}_2|$ are deformed moiré lattice vectors. LDOS, local density of states.

see a similar cascade of SBCI state on the electron-doping side (Supplementary Fig. 7).

Hartree–Fock calculations at finite magnetic field

We perform in-field self-consistent Hartree–Fock calculations of the interacting Bistritzer–MacDonald Hamiltonian at twist angle $\theta = 1.05°$ and crucially include uniaxial heterostrain $\varepsilon = 0.2\%$ (see Supplementary Information for details). Figure 3a shows the calculated phase diagram of the incompressible states formed between magnetic flux $\Phi/\Phi_0 = 1/12$ and 1/2, with the marker radius denoting the size of the associated charge gap. We further characterize each data point by examining the wavefunction, isospin symmetry and moiré translational symmetry (Supplementary Fig. 8) and group them according to their topological indices (t, s). States with the largest energy gaps form the main sequence of the CCI states with $|t| = 1$, 2 and 3 and $|s| = 3$, 2 and 1, respectively, as well as the integer quantum Hall states with $|t| = 4$, 3, 2 and 1 and $|s| = 0$ (denoted as purple). The black markers represent the topologically trivial correlated insulators at $|s| = 2$ and 3, which correspond to the states marked by the black lines in Fig. 1g. These $t = 0$ states are adiabatically connected to the zero-field ground state (marked by magenta in Fig. 1g), which are now commonly believed to be incommensurate Kekulé spiral states in the presence of strain[33,34]. A detailed theoretical analysis of the $|s| = 3$ and 2 states also reveals their incommensurate Kekulé spiral state like isospin symmetry-breaking (Supplementary Fig. 9).

The calculation predicts a series of Chern insulators with $|t| = 1$, 2 and 3 and $|s| = 5/2$, 3/2 and 1/2, denoted in red, along with a (−3, −2/3) state with a smaller energy gap. All correspond to SBCI states seen in our Landau fan. Figure 3b shows the calculated energy spectrum of the (−3, −1/2) SBCI gap as a function of magnetic flux (Supplementary Fig. 10). The interaction-driven gap size changes non-monotonically with magnetic field, with an apparent energy gap opening for $\Phi/\Phi_0 > 1/8$ and closing for $\Phi/\Phi_0 \approx 1/2$. The calculated local density of states at the edge of the gap exhibits a real-space charge modulation that forms a stripe-like feature (Fig. 3c and Supplementary Fig. 11). The fractional filling factor s, non-zero Chern number $|t|$ and the broken moiré translational symmetry are all consistent with our interpretation of these states as SBCIs.

Overall, we find good qualitative agreement between our theoretical calculations and the experimental phase diagram. This can be further demonstrated by comparing the calculated and measured energy gaps of the three half-integer SBCIs (Fig. 3a inset versus Fig. 2e inset). Although the experimentally measured transport gaps are probably underestimated due to the presence of (twist angle) disorder[35], we find they follow the same relative hierarchy as in the calculation. In addition, the calculated phase diagram is robust against perturbations from the proximity-induced spin–orbit coupling of the adjacent WSe_2 layer as well as from small changes to the graphene–graphene twist angle (Supplementary Figs. 12 and 13). Our Hartree–Fock calculations also predict intervalley coherence underlying the SBCI states (Supplementary Fig. 14), much like the parent CCI states. Future microscopic studies using scanning tunnelling microscopy will be critical for revealing the broken moiré translational symmetry and exploring the potential Kekulé pattern[34] of the SBCI states.

Unconventional FQH in magnetic sub-bands

We next discuss the observation of FQH states and highlight their unconventional nature. Figure 4a shows a map of ρ_{xx} at high field, where

https://doi.org/10.1038/s41567-025-02997-4

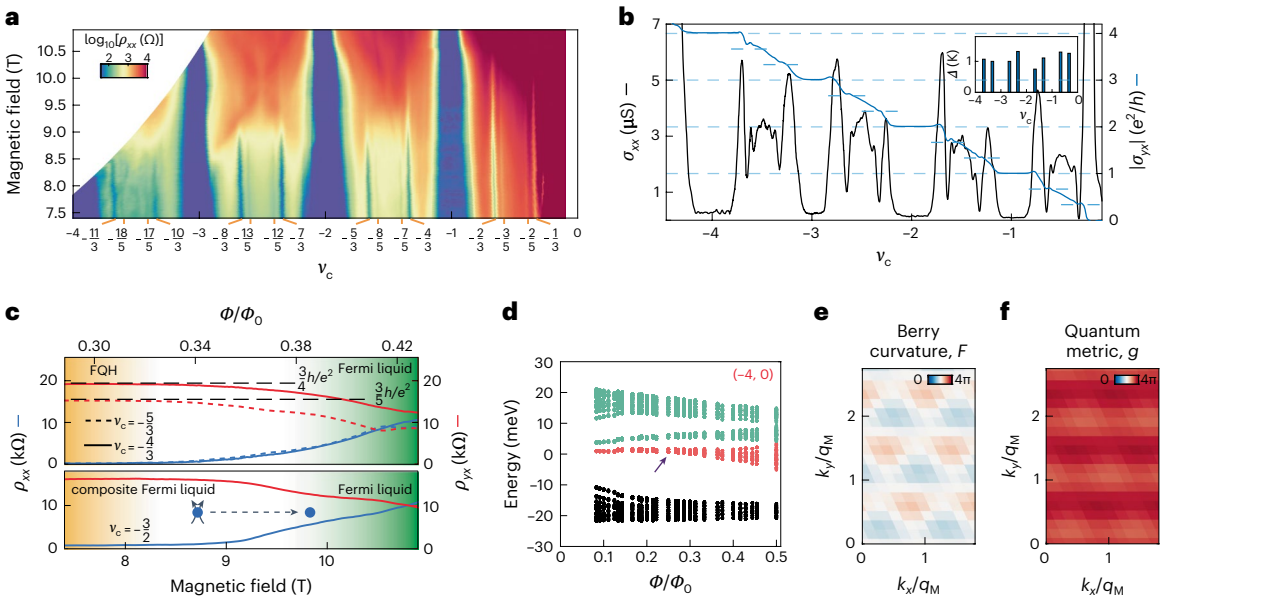

Fig. 4 | Unconventional FQH states in magnetic sub-bands with finite bandwidth. a, Zoom-in measurement of the ρ_{xx} Landau fan (taken from a different contact pair than in Fig. 1f, as shown in Supplementary Fig. 3), plotted against ν_c. **b**, σ_{xx} (left y axis) and σ_{yx} (right y axis) measured at $B = 7$ T. Inset: measured thermal activation gaps of the FQH states with denominator 3. **c**, ρ_{xx} and ρ_{yx} measured as a function of B at $\nu_c = -5/3$ and $-4/3$ (top) and $\nu_c = -3/2$ (bottom). The FQH states and composite Fermi liquid at low magnetic field transition to a normal Fermi liquid at high magnetic field. **d**, Calculated interacting Hofstadter spectrum when the Fermi energy is in the gap of the (−4, 0) state. Occupied states are marked by black, and unoccupied states are marked by green and red. The red bands are the magnetic sub-band hosting the observed FQH states. **e**,**f**, Berry curvature $\mathcal{F}$ (**e**) and quantum metric g (**f**) of the red magnetic sub-band, calculated at $\Phi/\Phi_0 = 1/4$ (purple arrow in **d**). q_M is defined following $q_M \equiv \sqrt{|\mathbf{g}_1||\mathbf{g}_2|}/q$ at flux ratio $\Phi/\Phi_0 = p/q$. $|\mathbf{g}_1|$ and $|\mathbf{g}_2|$ are deformed moiré reciprocal lattice vectors.

we observe FQH states at certain partial fillings of each magnetic sub-band with effective filling factors $\tilde{\nu_c} = \nu_c - [\nu_c] = 1/3, 2/5, 3/5$ and $2/3$, where $\nu_c = n\Phi_0/B$ is the LL filling fraction. These fillings are consistent with the usual Jain sequence[23], as is generally observed in the lowest LL with orbital number $N = 0$. Figure 4b shows line cuts of σ_{yx} and the longitudinal conductivity, $\sigma_{xx} = \rho_{xx}/(\rho_{yx}^2 + \rho_{xx}^2)$, at $B = 7$ T, which exhibits nearly quantized $\sigma_{yx} = \nu_c e^2/h$ at $\nu_c = -1/3, -2/3, -4/3, -5/3, -7/3$ and $-8/3$. The values of σ_{yx} at $\nu_c = -10/3, -11/3$ deviate from their anticipated values due to mixing with the larger residual σ_{xx}. The inset of Fig. 4b shows measurements of the thermal activation gaps of the FQH states with denominator 3 (Supplementary Fig. 15). All gaps are close to 1 K and, in certain cases, do not respect particle–hole symmetry relative to half-filling. These energy gaps are one order of magnitude smaller than those in Laughlin states at $\nu_c = 1/3$ or $2/3$ in monolayer[36–40] and bilayer graphene[41–45]. They are about $0.01E_c$, assuming Coulomb energy $E_c = e^2/4\pi\varepsilon\varepsilon_0 l_B$ with effective dielectric constant $\varepsilon \approx 15$, where ε is vacuum permittivity. Besides the inevitable moiré disorder[35], which is absent in crystalline graphene, the FQH energy gaps could also be weakened by a competing Fermi liquid phase due to the finite bandwidth of the magnetic sub-bands or by charge/spin density wave instabilities due to strain and non-uniform quantum geometry.

The FQH states disappear at high magnetic fields (above approximately 8.5–10 T). This is distinct from the usual case of LLs, where the FQH gaps scale with the strength of the Coulomb interactions and, thus, monotonically increase with the magnetic field. Figure 4c shows line cuts of ρ_{xx} and ρ_{yx} as a function of B, showing the evolution of FQH states at $\nu_c = -4/3$ and $-5/3$ (top panel) into a gapless Fermi liquid. We see similar crossover behaviour at half-filling, $\nu_c = -3/2$ (bottom panel), which is a putative composite Fermi liquid when flanked by FQH states. Both panels show a smooth phase transition from the Jain-sequence FQH states to a dissipative Fermi liquid phase as B increases (Supplementary Fig. 16). Intuitively, this can be understood as the FQH states becoming destabilized by the broadened bandwidth at a higher magnetic field and eventually losing the competition to a normal Fermi liquid.

Similar non-monotonic behaviour of FQH states was previously observed in aligned graphene/hBN[3,4], yet little is known about the nature of these states. In moiré lattices, FQH states appear at partial filling of the interaction-renormalized magnetic sub-bands emanating from the charge neutrality point. For MATBG, these are commonly referred to as the zero-energy LLs, but despite their name, the corresponding energy bands are, in fact, distinct from LLs due to the non-uniform distribution of the Berry curvature. Rather, they are strongly influenced by the moiré pattern and should be thought of as magnetic sub-bands within the Hofstadter butterfly. They feature finite dispersion and arise by hybridizing different low-energy LLs from the charge neutrality point of the two graphene layers. As a result, they may differ substantially from the physics of the $N = 0$ lowest LL[46], even when they have the same Chern number, as we elaborate upon below.

Figure 4d shows the interaction-renormalized energy spectrum with the Fermi energy in the gap of the (−4, 0) state. Red denotes the magnetic sub-bands hosting the observed FQH states. Although a detailed theoretical modelling of the FQHs by exact diagonalization is beyond the scope of this work, we qualitatively evaluate their nature by inspecting the quantum geometry of the relevant magnetic sub-bands. We adopt the notion of ideal quantum geometry indicators[47], which evaluate the similarity of the sub-band with the $N = 0$ LL (see Supplementary Information for details), and we calculate whether the magnetic sub-bands are close to the ideal conditions needed for hosting fractionalized states. We note that these indicators provide only a basic framework for predicting the presence of fractionalized states but are not strictly necessary and sufficient conditions, as the formation of such states depends on Coulomb interactions in addition to the quantum geometry of the band. Figure 4e,f shows the distribution of the imaginary part of the quantum geometry η (Berry curvature $\mathcal{F}$) and the real part of η (quantum metric g) of the red magnetic sub-bands. Notably, both $\mathcal{F}$ and g exhibit a non-uniform profile within the magnetic Brillouin zone, distinct from the $N = 0$ LL with a uniform distribution of the value 2π. The uniformity of $\mathcal{F}$ is measured

by its standard deviation, $\sigma(\mathcal{F}) \approx 0.113$, which is finite, unlike that for the $N = 0$ LL, but nevertheless, relatively small[48]. The trace condition measures the similarity of the wavefunctions of the sub-bands to the $N = 0$ LL and is found to be $T(\eta) \approx 4.226$ (see Supplementary Information for details). In contrast to the relatively uniform Berry curvature distribution, the large trace condition indicates dissimilarity with the lowest LL (where $T(\eta) = 0$).

Conclusion

Nearly uniform Berry curvature is known to support fractionalized states, allowing us to rationalize the appearance of the Jain-sequence FQH states even in bands unlike the lowest LL. This is further confirmed by the decomposition of the magnetic sub-bands into the basis of the LLs of monolayer graphene (Supplementary Fig. 17), from which we find that most of the contribution comes from LLs with $N \neq 0$. Despite their emanation from the charge neutrality point like conventional FQH states, our calculations indicate that the fractionalized states are closer to in-field FCIs from a lattice Chern band. These states require a magnetic field to form and arise despite the quantum geometric non-idealities of the magnetic sub-bands, including their finite bandwidth, quantum metric fluctuations and the small gaps to nearby bands. Similar arguments should be applicable to an entire class of FQH states in moiré superlattices where the quantum geometry is non-uniform and the magnetic length is comparable to the superlattice period. Direct evidence of the non-trivial quantum geometry properties of the MATBG Hofstadter sub-bands awaits future experimental confirmation using probes such as nonlinear transport[49,50], optical high harmonic generation[51], dichroic angle-resolved photoemission spectroscopy[52] or the circular photogalvanic effect[53] at infrared or terahertz frequency.

Online content

Any methods, additional references, Nature Portfolio reporting summaries, source data, extended data, supplementary information, acknowledgements, peer review information; details of author contributions and competing interests; and statements of data and code availability are available at https://doi.org/10.1038/s41567-025-02997-4.

References

1. Hofstadter, D. R. Energy levels and wave functions of Bloch electrons in rational and irrational magnetic fields. *Phys. Rev. B* **14**, 2239–2249 (1976).
2. Wannier, G. H. A result not dependent on rationality for Bloch electrons in a magnetic field. *Phys. Status Solidi B* **88**, 757–765 (1978).
3. Wang, L. et al. Evidence for a fractional fractal quantum Hall effect in graphene superlattices. *Science* **350**, 1231–1234 (2015).
4. Spanton, E. M. et al. Observation of fractional Chern insulators in a van der Waals heterostructure. *Science* **360**, 62–66 (2018).
5. Bistritzer, R. & MacDonald, A. H. Moiré bands in twisted double-layer graphene. *Proc. Natl Acad. Sci. USA* **108**, 12233–12237 (2011).
6. Cao, Y. et al. Correlated insulator behaviour at half-filling in magic-angle graphene superlattices. *Nature* **556**, 80–84 (2018).
7. Cao, Y. et al. Unconventional superconductivity in magic-angle graphene superlattices. *Nature* **556**, 43–50 (2018).
8. Yankowitz, M. et al. Tuning superconductivity in twisted bilayer graphene. *Science* **363**, eaav1910 (2019).
9. Lu, X. et al. Superconductors, orbital magnets and correlated states in magic-angle bilayer graphene. *Nature* **574**, 653–657 (2019).
10. Sharpe, A. L. et al. Emergent ferromagnetism near three-quarters filling in twisted bilayer graphene. *Science* **365**, 605–608 (2019).
11. Serlin, M. et al. Intrinsic quantized anomalous Hall effect in a moiré heterostructure. *Science* **367**, 900–903 (2020).
12. Xie, Y. et al. Fractional Chern insulators in magic-angle twisted bilayer graphene. *Nature* **600**, 439–443 (2021).
13. Saito, Y. et al. Hofstadter subband ferromagnetism and symmetry-broken Chern insulators in twisted bilayer graphene. *Nat. Phys.* **17**, 478–481 (2021).
14. Yu, J. et al. Correlated Hofstadter spectrum and flavour phase diagram in magic-angle twisted bilayer graphene. *Nat. Phys.* **18**, 825–831 (2022).
15. Polshyn, H. et al. Topological charge density waves at half-integer filling of a moiré superlattice. *Nat. Phys.* **18**, 42–47 (2021).
16. He, M. et al. Symmetry-broken Chern insulators in twisted double bilayer graphene. *Nano Lett.* **23**, 11066–11072 (2023).
17. Park, J. M., Cao, Y., Watanabe, K., Taniguchi, T. & Jarillo-Herrero, P. Flavour Hund's coupling, Chern gaps and charge diffusivity in moiré graphene. *Nature* **592**, 43–48 (2021).
18. Nuckolls, K. P. et al. Strongly correlated Chern insulators in magic-angle twisted bilayer graphene. *Nature* **588**, 610–615 (2020).
19. Choi, Y. et al. Correlation-driven topological phases in magic-angle twisted bilayer graphene. *Nature* **589**, 536–541 (2021).
20. Das, I. et al. Symmetry-broken Chern insulators and Rashba-like Landau-level crossings in magic-angle bilayer graphene. *Nat. Phys.* **17**, 710–714 (2021).
21. Wu, S., Zhang, Z., Watanabe, K., Taniguchi, T. & Andrei, E. Y. Chern insulators, van Hove singularities and topological flat bands in magic-angle twisted bilayer graphene. *Nat. Mater.* **20**, 488–494 (2021).
22. Wang, X. & Vafek, O. Theory of correlated Chern insulators in twisted bilayer graphene. *Phys. Rev. X* **14**, 021042 (2023).
23. Jain, J. K. Composite-fermion approach for the fractional quantum Hall effect. *Phys. Rev. Lett.* **63**, 199–202 (1989).
24. Polski, R. et al. Hierarchy of symmetry breaking correlated phases in twisted bilayer graphene. Preprint at https://arxiv.org/abs/2205.05225 (2022).
25. He, M. et al. Dynamically tunable moiré exciton Rydberg states in a monolayer semiconductor on twisted bilayer graphene. *Nat. Mater.* **23**, 224–229 (2024).
26. Tschirhart, C. L. et al. Imaging orbital ferromagnetism in a moiré Chern insulator. *Science* **372**, 1323–1327 (2021).
27. Arora, H. S. et al. Superconductivity in metallic twisted bilayer graphene stabilized by WSe_2. *Nature* **583**, 379–384 (2020).
28. Lin, J.-X. et al. Spin-orbit–driven ferromagnetism at half moiré filling in magic-angle twisted bilayer graphene. *Science* **375**, 437–441 (2022).
29. Stepanov, P. et al. Competing zero-field Chern insulators in superconducting twisted bilayer graphene. *Phys. Rev. Lett.* **127**, 197701 (2021).
30. Grover, S. et al. Chern mosaic and Berry-curvature magnetism in magic-angle graphene. *Nat. Phys.* **18**, 885–892 (2022).
31. Tseng, C.-C. et al. Anomalous Hall effect at half filling in twisted bilayer graphene. *Nat. Phys.* **18**, 1038–1042 (2022).
32. Streda, P. Quantised Hall effect in a two-dimensional periodic potential. *J. Phys. C* **15**, L1299 (1982).
33. Kwan, Y. H. et al. Kekulé spiral order at all nonzero integer fillings in twisted bilayer graphene. *Phys. Rev. X* **11**, 041063 (2021).
34. Nuckolls, K. P. et al. Quantum textures of the many-body wavefunctions in magic-angle graphene. *Nature* **620**, 525–532 (2023).
35. Uri, A. et al. Mapping the twist-angle disorder and Landau levels in magic-angle graphene. *Nature* **581**, 47–52 (2020).
36. Bolotin, K. I., Ghahari, F., Shulman, M. D., Stormer, H. L. & Kim, P. Observation of the fractional quantum Hall effect in graphene. *Nature* **462**, 196–199 (2009).

37. Du, X., Skachko, I., Duerr, F., Luican, A. & Andrei, E. Y. Fractional quantum Hall effect and insulating phase of Dirac electrons in graphene. *Nature* **462**, 192–195 (2009).
38. Ghahari, F., Zhao, Y., Cadden-Zimansky, P., Bolotin, K. & Kim, P. Measurement of the ν=1/3 fractional quantum Hall energy gap in suspended graphene. *Phys. Rev. Lett.* **106**, 046801 (2011).
39. Dean, C. R. et al. Multicomponent fractional quantum Hall effect in graphene. *Nat. Phys.* **7**, 693–696 (2011).
40. Feldman, B. E., Krauss, B., Smet, J. H. & Yacoby, A. Unconventional sequence of fractional quantum Hall states in suspended graphene. *Science* **337**, 1196–1199 (2012).
41. Kou, A. et al. Electron-hole asymmetric integer and fractional quantum Hall effect in bilayer graphene. *Science* **345**, 55–57 (2014).
42. Maher, P. et al. Tunable fractional quantum Hall phases in bilayer graphene. *Science* **345**, 61–64 (2014).
43. Li, J. I. A. et al. Even-denominator fractional quantum Hall states in bilayer graphene. *Science* **358**, 648–652 (2017).
44. Zibrov, A. A. et al. Tunable interacting composite fermion phases in a half-filled bilayer-graphene Landau level. *Nature* **549**, 360–364 (2017).
45. Huang, K. et al. Valley isospin controlled fractional quantum Hall states in bilayer graphene. *Phys. Rev. X* **12**, 031019 (2022).
46. Haldane, F. D. M. Fractional quantization of the Hall effect: a hierarchy of incompressible quantum fluid states. *Phys. Rev. Lett.* **51**, 605–608 (1983).
47. Roy, R. Band geometry of fractional topological insulators. *Phys. Rev. B* **90**, 165139 (2014).
48. Parker, D. et al. Field-tuned and zero-field fractional Chern insulators in magic angle graphene. Preprint at https://arxiv.org/abs/2112.13837 (2021).
49. Wang, N. et al. Quantum-metric-induced nonlinear transport in a topological antiferromagnet. *Nature* **621**, 487–492 (2023).
50. Gao, A. et al. Quantum metric nonlinear Hall effect in a topological antiferromagnetic heterostructure. *Science* **381**, 181–186 (2023).
51. Luu, T. T. & Wörner, H. J. Measurement of the Berry curvature of solids using high-harmonic spectroscopy. *Nat. Commun.* **9**, 916 (2018).
52. Schüler, M. et al. Local Berry curvature signatures in dichroic angle-resolved photoelectron spectroscopy from two-dimensional materials. *Sci. Adv.* **6**, eaay2730 (2020).
53. de Juan, F., Grushin, A. G., Morimoto, T. & Moore, J. E. Quantized circular photogalvanic effect in Weyl semimetals. *Nat. Commun.* **8**, 15995 (2017).

Publisher's note Springer Nature remains neutral with regard to jurisdictional claims in published maps and institutional affiliations.

Springer Nature or its licensor (e.g. a society or other partner) holds exclusive rights to this article under a publishing agreement with the author(s) or other rightsholder(s); author self-archiving of the accepted manuscript version of this article is solely governed by the terms of such publishing agreement and applicable law.

© The Author(s), under exclusive licence to Springer Nature Limited 2025

Methods

Sample fabrication

Heterostructures of graphite/hBN/WSe_2/MATBG/hBN/graphite were assembled using a standard dry-transfer technique with a polycarbonate/polydimethylsiloxane stamp and transferred onto a Si/SiO_2 wafer. The MATBG stack was fabricated using the tear-and-stack method. We used 3–5 nm of graphite as the bottom gates, and 3–5 layers of graphene were used for the top gate to minimize its optical absorption. We had no intentional control over the twist angle between WSe_2 and its adjacent graphene layer during the stacking process. CHF_3/O_2 and O_2 plasma etching followed by electron-beam lithography were used to define a Hall bar geometry, and Cr/Au contacts (7 nm/70 nm) were finally added using electron-beam evaporation.

Transport measurements

Transport measurements were conducted in a Bluefors dilution refrigerator. Measurements were performed with a 1–5 nA a.c. excitation current at either 13.3 or 13.7 Hz. The current and voltage were pre-amplified by DL 1211 and SR560 amplifiers, respectively, and then read out by SR830/SR860 lock-in amplifiers. The gate voltages were supplied by either NI DAQ or Keithley 2450. In this study, we used the bottom gate voltage V_b to control the carrier density $n = V_bC_b/e$, where C_b is the bottom gate capacitance per unit area. A global Si gate voltage was applied to reduce the contact resistance.

The filling factor ν is defined as the number of electrons per moiré unit cell. Full filling of the eightfold-degenerate flat bands in twisted bilayer graphene corresponds to four electrons or holes per moiré unit cell, $\nu = \pm 4$. The carrier densities corresponding to the full fillings $\nu = \pm 4$ were determined by measuring the Hall coefficient at a small magnetic field B, $R_H = [\rho_{xy}(B) - \rho_{xy}(-B)]/(2B)$. The Hall carrier density, $n_H = 1/eR_H$, reverses the carrier type (from electron to hole or vice versa) across the full fillings $\nu = \pm 4$ and can be identified as the zero crossing in the R_H measurements. The twist angle was then determined from $n = 8\theta^2/\sqrt{3}a^2$, where $a = 0.246$ nm is the graphene lattice constant. The twist angle was confirmed by fitting the observed quantum Hall states and Chern insulators within the allowed Hofstadter states in the Wannier diagram.

Data availability

Source data are provided with this paper. All other data are available from the corresponding authors upon reasonable request.

Code availability

The code used for the data analysis in this study is available from the corresponding authors upon reasonable request.

Acknowledgements

The work at UW is supported by NSF MRSEC DMR-2308979. M.H. acknowledges support from the Princeton quantum initiative. X.W. acknowledges support from the National High Magnetic Field Laboratory through NSF Grant No. DMR-2128556 and the State of Florida. B.A.B. was supported by Simons Investigator Grant No. 404513. B.A.B. and O.V. are supported by the Gordon and Betty Moore Foundation's EPiQS Initiative (Grant No. GBMF11070). K.W. and T.T. acknowledge support from the JSPS KAKENHI (Grant Nos. 21H05233 and 23H02052) and the World Premier International Research Center Initiative, MEXT, Japan.

Author contributions

M.H. fabricated the devices. M.H. and J.C. performed the measurements and analysed the data supervised by M.Y. and X.X. X.W. performed the theoretical calculations supervised by O.V., with theory inputs from J.H.-A., R.P., A.S. and B.A.B. K.W. and T.T. grew the hBN crystals. M.H., X.W., M.Y., O.V. and X.X. wrote the paper with input from all authors.

Competing interests

The authors declare no competing interests.

Additional information

Supplementary information The online version contains supplementary material available at https://doi.org/10.1038/s41567-025-02997-4.

Correspondence and requests for materials should be addressed to Minhao He, Matthew Yankowitz, Oskar Vafek or Xiaodong Xu.

Peer review information *Nature Physics* thanks the anonymous reviewers for their contribution to the peer review of this work.

Reprints and permissions information is available at www.nature.com/reprints.